Crystal-field Stark effect on the upconversion light emission spectrum of α-$NaYF_4$ nanoparticles doped with Dy^{3+}, Er^{3+}, or Yb^{3+}

A. F. García-Flores,[1] E. D. Martínez,[2,3,4] J. Munevar,[5] D. J. Garcia,[3,4] P. S. Cornaglia,[2,3,4] F. Fabris,[1] R. R. Urbano,[1] and C. Rettori[1]

[1]*Instituto de Física "Gleb Wataghin", UNICAMP, Campinas, São Paulo 13083-970, Brazil*
[2]*Instituto de Nanociencia y Nanotecnología (INN), San Carlos de Bariloche, CP 8400 Río Negro, Argentina*
[3]*Consejo Nacional de Investigaciones Científicas y Técnicas (CONICET), San Carlos de Bariloche, CP 8400 Río Negro, Argentina*
[4]*Centro Atómico Bariloche and Instituto Balseiro, Comisión Nacional de Energía Atómica (CNEA), CP 8400 Bariloche, Argentina*
[5]*CCNH, Universidade Federal do ABC (UFABC), Santo André, São Paulo 09210-580, Brazil*

(Received 22 June 2022; accepted 9 September 2022; published 30 September 2022)

$NaYF_4$ nanoparticles (NPs) form in two crystal structures, cubic (α-phase) and hexagonal (β-phase), each one presenting a different crystal electric field (CEF) Stark effect, that affects the upconversion (UC) light emission of the NPs when doped with rare-earth elements. Therefore, the knowledge of the CEF parameters, the wave functions, and energy levels of the rare earth (RE) J-multiplet is expected to be of great help for the understanding and improvement of the UC light emission. In this work, α-phase $NaYF_4$ NPs doped with Dy^{3+}, Er^{3+}, or Yb^{3+} were investigated by means of magnetization, electron spin resonance (ESR), and optical spectroscopy techniques. Fittings of the temperature- and magnetic-field-dependent magnetization were performed to determine the fourth- and sixth-order cubic CEF parameters, B_4 and B_6. The ground state of Er^{3+}, Yb^{3+}, and Dy^{3+} in these α-$NaYF_4$ NPs was confirmed by low-temperature ESR experiments. The obtained CEF parameters were used to write down a total Hamiltonian that allows to determine the CEF Stark splitting for all energy levels of the REs $4f$ unfilled shell. We give details of how the Stark effect affects the overall energy splitting of the various J-multiplets and may explain the fine structure of the UC light emission in these cubic $NaY_{1-\delta}RE_\delta F_4$ NPs.

DOI: 10.1103/PhysRevB.106.125427

I. INTRODUCTION

At the end of the 20th century, a significant part of the condensed matter scientific community focused their attention on the nanoscale properties of materials. Granqvist *et al.* in 1976 observed experimentally for the first time the size dependence of optical properties in Al nanoparticles (NPs) [1]. Since then, many studies were carried out in this field unveiling many applications for NPs. Currently, this is still a young developing and very promising area [2,3]. Over the last decade, studies on upconversion (UC) phosphors have grown quickly due to their numerous applications in low-intensity IR imaging, three-dimensional flat-panel displays, solid-state lasers bioprobes, and bioimages [4–6] among others [7]. The UC phenomenon is a nonlinear optical process that involves a higher-energy photoemission originated by either a single ion undergoing a successive excitation by lower-energy photons or a process of energy transference between UC ions [8,9].

Lately, $NaYF_4$ NPs have been largely studied and it has been shown that among the UC phosphors, hexagonal $NaYF_4$ NPs are the most efficient host material for green and blue UC light emission when codoped with Yb^{3+} and Er^{3+}/Tm^{3+} ions [10]. $NaYF_4$ NPs form in either hexagonal phase (β-phase) or cubic phase (α-phase). It is known that the α-phase of this NPs presents very low UC light emission intensity as compared with that of the β-phase. Since both phases exhibit different UC intensities (quantum efficiency) and linewidths, it is evident that the atomic lattice arrangement plays an important role in the UC light emission of these NPs [11].

II. THEORETICAL FRAMEWORK

Rare earth (RE) elements diluted in host NPs experience the effect of the surrounding charges, i.e., the crystal electric field (CEF) effect. CEF splits the energy levels of the RE ions, i.e., crystal-field Stark effects [12], therefore, affecting the magnetic and optical properties of the NPs [13]. In fact, for half-integer-spin RE ions, CEF always leave a set of degenerated doublets or quadruplets (Kramer's degeneracy), which can be split by the application of a magnetic field, i.e., the Zeeman effect, and a microwave transition may be induced in an electron spin resonance (ESR) experiment. It is now well known how the magnetic response of diluted REs is affected by the CEF. At low-T, the magnetic susceptibility deviates from the expected high-T Curie-Weiss law. Therefore, the strength of the CEF can be determined by the analysis of the low-T experimental magnetization data.

For a cubic point site symmetry the CEF Hamiltonian can be written in terms of fourth- and sixth-order Stevens' operators as follows [14]:

$$\mathcal{H}_{\mathrm{CEF}} = B_4\left(O_4^0 + 5O_4^4\right) + B_6\left(O_6^0 - 21O_6^4\right), \qquad (1)$$

where the parameters B_4 and B_6 determine the strength of the fourth- and sixth-order CEF terms, respectively, and can be obtained through magnetization experiments independently on the emission spectra measurements. The Stevens' operators O_α^β can be written in terms of the total angular momentum operators J, J_z, and $J_\pm$ [15,16].

It is convenient to write $\mathcal{H}_{\text{CEF}}$ as

$$\mathcal{H}_{\text{CEF}} = W\left[x\left(\frac{O_4}{F(4)}\right) + (1-|x|)\left(\frac{O_6}{F(6)}\right)\right], \tag{2}$$

where $O_4 = O_4^0 + 5O_4^4$ and $O_6 = O_6^0 - 21O_6^4$, and using the following parametrization:

$$B_4 = \frac{Wx}{F(4)}, \tag{3}$$

$$B_6 = \frac{W(1-|x|)}{F(6)}. \tag{4}$$

Here W gives the overall strength of the CEF and x measures the relative strength of B_4 and B_6. Finally, the parameters $F(4)$ and $F(6)$ depend only on the J-manifold [14].

Understanding the effect of CEF in NPs is very important for the tuning of their UC light emission properties. However, so far only a few studies on CEF effects have been realized on NPs [13,17]. In particular, the role of the size and shape of the NPs, the surface/volume ratio, the strain distribution, and charge entrapment remain unknown.

The aim of this work is to determine the CEF parameters in α-$NaY_{1-\delta}RE_\delta F_4$ (RE = Dy, Er, Yb) by means of magnetization and ESR measurements and to relate them with the UC light emission linewidth. Moreover, a Hamiltonian for these systems is also proposed to simulate the shape and fine structure of the UC light emission spectrum.

III. EXPERIMENT

Pure α-phase $NaY_{1-\delta}RE_\delta F_4$ NPs (RE = Dy^{3+}, Er^{3+}, and Yb^{3+}; nominal $\delta = 0.02$) were synthesized by the thermal decomposition method of trifluoroacetates as described in Ref. [18]. One mmol of $Na(CF_3COO)$ (98 %, Aldrich), 0.98 mmol of $Y(CF_3COO)_3$ (99.99 %, Aldrich), and 0.02 mmol of $RE(CF_3COO)_3$ were added to 6.4 mL of 1-octadecene (ODE, 90 %, Sigma-Aldrich), 3.15 mL of oleic acid (OA, technical grade, Sigma-Aldrich), and 3.3 mL of oleylamine (OLA, technical grade, Sigma-Aldrich) in a three-neck round bottom flask. The mixture was heated up to 100–120° C with vigorous magnetic stirring under a vacuum for 30 minutes in a temperature-controlled electromantle to eliminate the water and oxygen content. Then, under Ar gas flux, the solution was heated up to a final temperature of 310° C and maintained at this temperature for 60 minutes until the reaction was completed. The mantle was then turned off and the flask was allowed to cool down to room-T. Finally, the NPs were extracted by multiple steps of washing in an excessive amount of absolute ethanol at room-T followed by centrifugation.

Structural characterization was provided by powder x-ray diffraction (XRD) technique carried out in a D2 Phaser Bruker diffractometer with Cu Kα radiation ($\lambda = 1.5418$ Å). Size and morphology were evaluated by transmission electron microscopy (TEM; JEM 2100, accelerating voltage of 200 kV and a Carl Zeiss Libra 120 TEM equipped with a tungsten thermionic source operating at 80 kV).

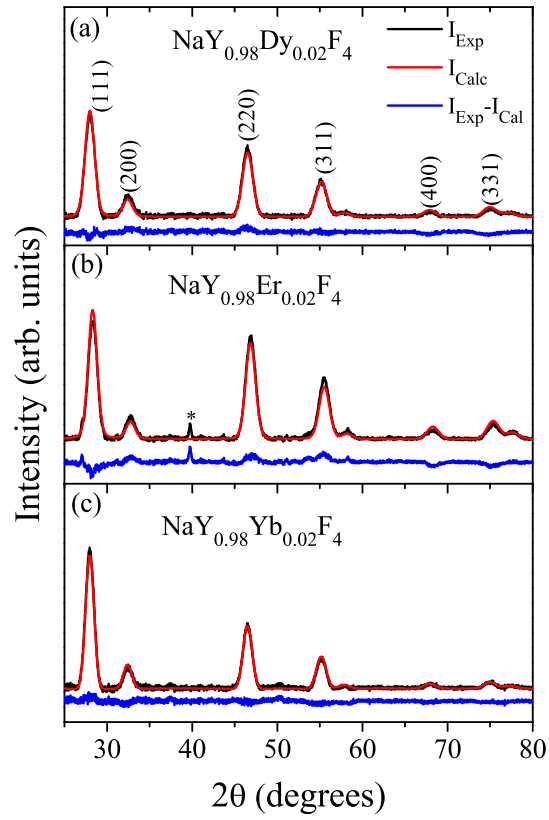

FIG. 1. Powder XRD patterns for α-phase $NaY_{0.98}Dy_{0.02}F_4$, $NaY_{0.98}Er_{0.02}F_4$, and $NaY_{0.98}Yb_{0.02}F_4$ nanoparticles. Peaks indexed according to the cubic structure of α-NaYF4, JCPDS card No. 77-2042. NaF impurity is indicated by asterisk.

The temperature dependence of magnetization was measured from 2 to 300 K at 2 kOe and 20 kOe and the magnetic field dependence at 2 K from 0 up to 70 kOe. dc-magnetization measurements were performed in a superconducting quantum interference-vibrating sample magnometer (SQUID-VSM) (Quantum Design MPMS3) and the diamagnetism of the sample holder and the $NaYF_4$ host lattice contributions were always taken into account. The continuous wave ESR measurements were accomplished in a Bruker ELEXSYS 500 spectrometer with the X-band frequency ($\nu = 9.48$ GHz) at low-T from 4 K to 50 K. The UC emission spectra of the samples were obtained at room-T with a QEPro Ocean Optics spectrometer under the continuous laser excitation of 980 nm.

IV. EXPERIMENTAL RESULTS

The powder XRD patterns of the $NaY_{1-\delta}RE_\delta F_4$ samples match with the expected peaks for the α-phase (space group: $Fm\bar{3}m$), as presented in Fig. 1. The width of the observed broad peaks for all three Dy, Er, and Yb doped samples are proportional to the size of the NPs according to the Scherrer's equation [19]. In addition, Rietveld refinement gave a

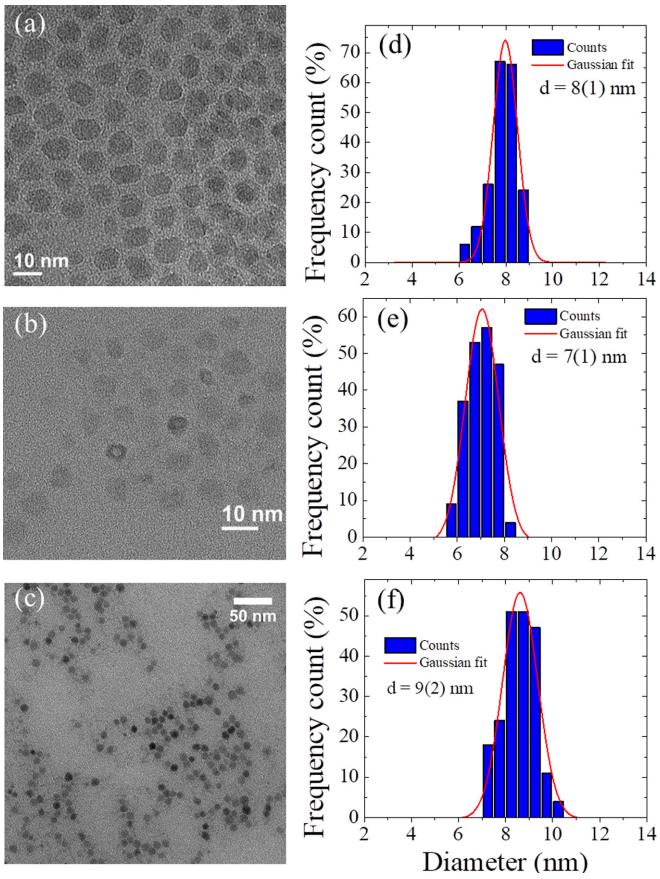

FIG. 2. (a)–(c) TEM images and (d)–(f) the size distribution histograms obtained from TEM images of ∼200 particles of α-phase $NaY_{0.98}Dy_{0.02}F_4$, $NaY_{0.98}Er_{0.02}F_4$ and $NaY_{0.98}Yb_{0.02}F_4$ nanoparticles, respectively. The mean sizes are indicated with the FWHM of the Gaussian distribution fitted to the data indicated in parentheses.

similar lattice parameter for them, with values of 5.517(2), 5.518(3), and 5.520(2) for $NaY_{0.98}Dy_{0.02}F_4$, $NaY_{0.98}Er_{0.02}F_4$, and $NaY_{0.98}Yb_{0.02}F_4$ NPs, respectively.

All prepared NPs presented polyhedral morphology and narrow size dispersion, see Fig. 2. The average size, around 8 nm for all three systems, was calculated by the Scherrer's equation using the XRD peak width of each sample and confirmed by TEM images. For the TEM images, the size dispersions are indicated in parentheses [see Figs. 2(d) to 2(f)], and were defined as full width at half maximum (FWHM) of the Gaussian distribution.

Figures 3(a) to 3(f) show the *dc*-magnetic susceptibility χ and χT at 2 and 20 kOe as a function of temperature for $NaY_{0.98}Dy_{0.02}F_4$, $NaY_{0.98}Er_{0.02}F_4$, and $NaY_{0.98}Yb_{0.02}F_4$ samples. The samples exhibit a Curie-Weiss behavior at temperatures above ∼150 K. By fitting the data above this temperature leads to a RE concentration (δ) of around 0.014 for Dy^{3+}, 0.012 for Er^{3+}, and 0.010 for Yb^{3+}, which are close to the nominal concentrations $\delta = 0.02$. The accuracy of these values may be strongly affected by the low signal/noise ratio at high temperatures though. Therefore, the samples are named with their nominal concentrations. Figure 4 presents the *dc*-magnetization as a function of the applied magnetic field up to 70 kOe.

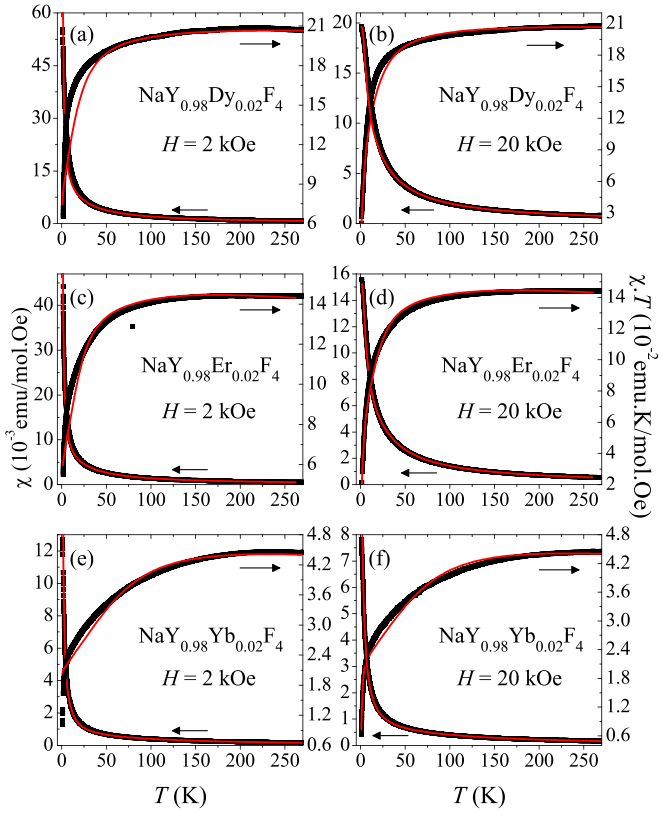

FIG. 3. T-dependence of the *dc*-magnetic susceptibility (χ) and $\chi.T$ for α-phase (a,b) $NaY_{0.98}Dy_{0.02}F_4$, (c,d) $NaY_{0.98}Er_{0.02}F_4$, and (e,f) $NaY_{0.98}Yb_{0.02}F_4$ NPs at 2 and 20 kOe. The solid red lines are best fits to Eq. (6) for cubic symmetry.

Figure 5 shows the ESR signals at different temperatures for the $NaY_{0.98}Dy_{0.02}F_4$, $NaY_{0.98}Er_{0.02}F_4$, and $NaY_{0.98}Yb_{0.02}F_4$ NPs. The intensity of the resonance follows a Curie-like behavior (insets of Fig. 5), indicating transitions within a Kramers' doublet ground state. The resonance spectra for the $NaY_{0.98}Er_{0.02}F_4$ NPs present a g-value of ∼6.80, close to the g-value of a Γ_7 ground state, and a line shape asymmetry with a broadening toward higher magnetic fields. This may indicate the presence of nearby anisotropic Γ_8 excited Kramers' states with lower g-values and also, presumably, admixture via magnetic field and/or strain, suggesting that the splitting between these levels should not be too large, probably of the order of ∼28 cm^{-1}. Now, the resonance spectra for the $NaY_{0.98}Yb_{0.02}F_4$ NPs present a g-value of ∼3.40 close to the g-value of a Γ_7 ground state and a nearly symmetric Lorentzian-like line shape, suggesting a rather well-isolated Γ_7 ground state. In the case of $NaY_{0.98}Dy_{0.02}F_4$, similarly to $NaY_{0.98}Er_{0.02}F_4$, the broadening toward higher magnetic field indicates the presence of nearby excited anisotropic Γ_8 (see Table I).

UC light emission spectrum for Er and Yb codoped NPs is presented in Fig. 6. The transition peaks are assigned to optical transitions matching the difference between the energy levels due to spin-orbit coupling. These results show broad transition lines with multiple peaks, suggesting that the CEF splits the $4f$ energy levels of the Er^{3+} ions diluted in the host NPs. We will show that this is in agreement with the energy

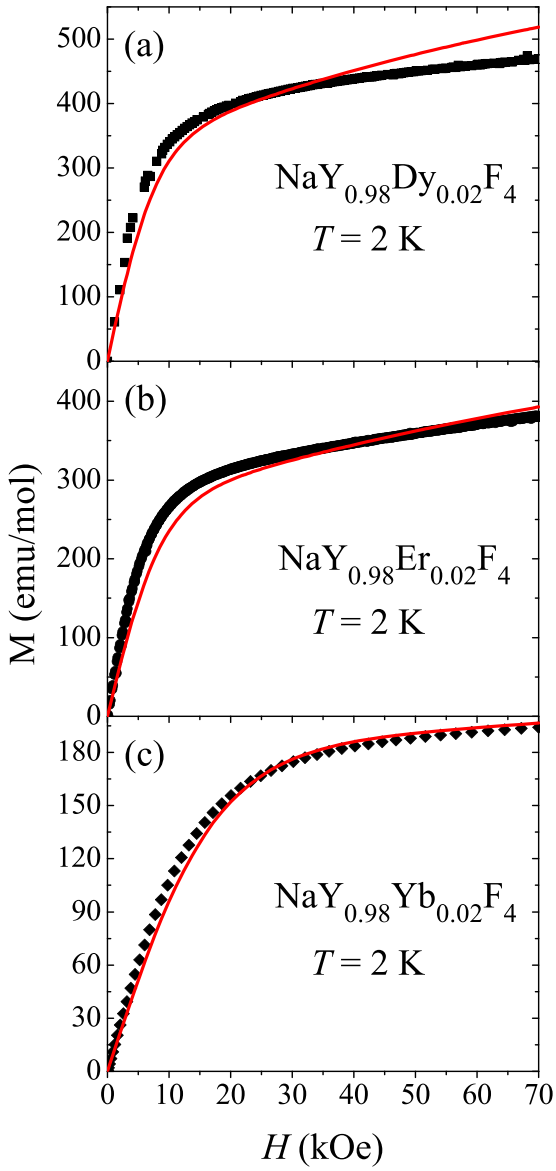

FIG. 4. H-dependent magnetization at 2 K for α-phase (a) $NaY_{0.98}Dy_{0.02}F_4$, (b) $NaY_{0.98}Er_{0.02}F_4$, and (c) $NaY_{0.98}Yb_{0.02}F_4$ NPs. The solid red lines are best fits to Eq. (6) in cubic symmetry.

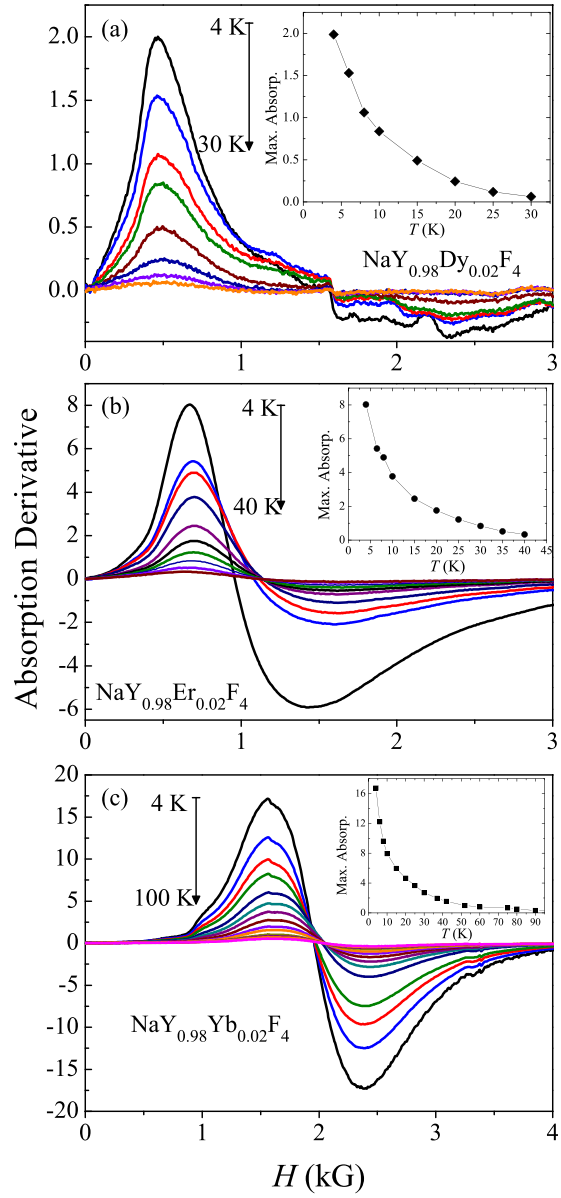

FIG. 5. X-band ESR spectra for α-phase (a) $NaY_{0.98}Dy_{0.02}F_4$, (b) $NaY_{0.98}Er_{0.02}F_4$, and (c) $NaY_{0.98}Yb_{0.02}F_4$ NPs at different temperatures. The insets show the T-dependence of the low-field resonance maximum.

levels predicted by the magnetization data for the Er^{3+} $J = 15/2$ ground state, shown in Table I. This will be discussed further in the next section considering the energy splitting of the Er^{3+} excited states due to the CEF.

V. ANALYSIS AND DISCUSSION

The Hamiltonian considered in our analysis of magnetization and susceptibility involves the Stark effect of the CEF contribution for a single ion on cubic local symmetry and also the Zeeman interaction due to the magnetic field applied. The CEF splits the J-multiplets of the RE ions into a set of two- and fourfold Kramers' degenerate energy levels. Kramers' doublets or quadruplets have their degeneracy lifted by the application of a magnetic field. The Hamiltonian of the system in the absence of strains is written as

$$\mathcal{H} = \mu_B g_J \vec{H} \cdot \vec{J} + \mathcal{H}_{\text{CEF}}, \tag{5}$$

TABLE I. Eigenenergies E_i (cm^{-1}), and the corresponding eigenfunctions ϕ_i of the ground state J-multiplet split due to cubic CEF effect for the Dy^{3+}, Er^{3+}, and Yb^{3+} ions.

RE Ion	E_i	ϕ_i	RE Ion	E_i	ϕ_i	RE Ion	E_i	ϕ_i
	0	Γ_7		0	Γ_7		0	Γ_7
	31	$\Gamma_8^{(1)}$		48	$\Gamma_8^{(1)}$			
Dy^{3+}	78	$\Gamma_8^{(2)}$	Er^{3+}	58	Γ_6	Yb^{3+}	144–190	Γ_8
	204	Γ_6		222	$\Gamma_8^{(2)}$			
	268	$\Gamma_8^{(3)}$		263	$\Gamma_8^{(3)}$		211–225	Γ_6

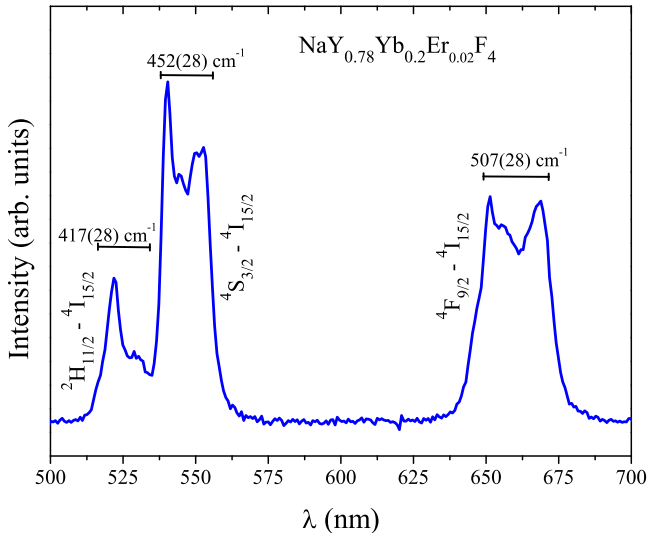

FIG. 6. UC light emission spectrum for co-doped α-$NaY_{0.78}Yb_{0.2}Er_{0.02}F_4$ nanoparticles.

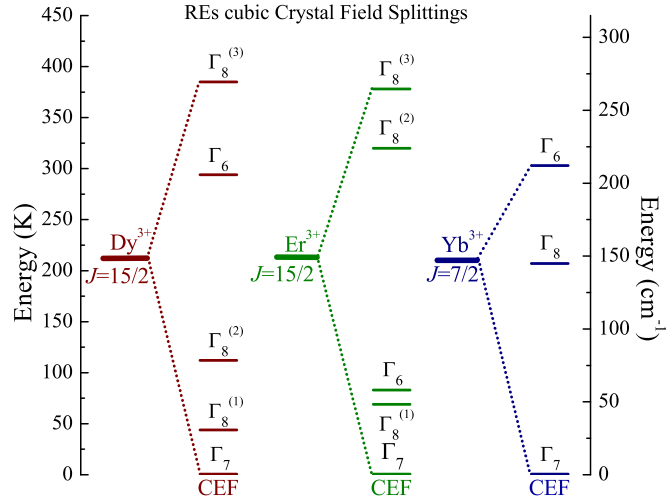

FIG. 7. Scheme of the ground state J-multiplet for Dy^{3+}, Er^{3+}, and Yb^{3+} due to the cubic CEF effect in α-$NaYF_4$.

where μ_B is the Bohr magneton, g_J is the Landé factor, $\vec{H}$ is the external magnetic field, $\vec{J}$ is the total angular momentum, and $\mathcal{H}_{\rm CEF}$ is the CEF contribution to the Hamiltonian [see Eq. (1)]. Once the energy levels are split by the CEF and the magnetic field, the resultant magnetization depends on the thermal population of the energy levels (Boltzmann distribution). Hence, it is written as

$$M(H,T) = \frac{\sum_{i=1}^{2J+1} m_i(H) e^{-E_i(H)/k_BT}}{\sum_{i=1}^{2J+1} e^{-E_i(H)/k_BT}}, \tag{6}$$

where $E_i(H)$ and $m_i(H)$ are the energy eigenvalue and magnetization of each eigenstate of the Hamiltonian in Eq. (5) as a function of the applied magnetic field and temperature. Then, by fitting the experimental dc-magnetization data to Eq. (6) as a function of H (0 to 70 kOe) and T (2 K to 250 K), we find the CEF parameters B_n^m for the RE-doped NPs. The results are displayed in Table II. For Yb^{3+} the relatively large energy of the first excited state (approximately above 140 cm^{-1}) makes it difficult to assign a single value for the fitting parameter (see energy levels in Table I and Fig. 7). Instead a range for B_6 is found. Figure 8 shows the Lea, Leask, and Wolf energy diagrams [14] for cubic symmetry with the eigenenergies for Dy^{3+}, Er^{3+}, and Yb^{3+} doped NPs corresponding to the B_4 and B_6 parameters of Table II obtained from the dc-magnetization data. It is clear that small x variations lead to large changes for Er^{3+} and Dy^{3+} ions while for Yb^{3+} it leaves a well-isolated doublet and does not affect low-temperature properties.

The parameters A_n^m in Table II represent the CEF effects on the RE ion site due to the charges of the neighboring ions in the host NPs. These parameters are almost independent of RE [20,21] and can be related to the B_n^m, which are RE-dependent parameters by

$$B_n^m = \langle r^n \rangle A_n^m \theta_n, \tag{7}$$

where $\langle r^n \rangle$ are the average radii over the $4f$ shell for each RE. θ_n are multiplicative factors ($\theta_4 = \beta_J$ and $\theta_6 = \gamma_J$) evaluated for each RE ion [16]. The A_n^m parameters might present a dependence on the atomic number Z and, as an often used approximation, we also consider them as RE independent [13,15].

Using the parameters from Table II, the calculated eigenstates lead to a Γ_7 doublet ground state for the three REs ($J = 15/2$ for Er^{3+}, Dy^{3+}, and $J = 7/2$ for Yb^{3+}) in these NPs. Notice that for Er and Dy doped NPs, the first excited state $\Gamma_8^{(1)}$ is close to the Γ_7 ground state. This proximity makes these excited states accessible for thermal excitations at low-T and may explain the asymmetric broadening toward higher fields (lower g-values) of the ESR powder-like spectra

TABLE II. CEF parameters B_n, δ (concentration), x [from Eqs. (3) and (4)] and A_n (see Sec. V) for Dy^{3+}, Er^{3+}, and Yb^{3+} in α-$NaYF_4$, obtained from the fittings of the T-dependence of the dc-magnetization data.

RE ion	B_4 (mK)	B_6 (mK)	δ	x	W (K)
Dy^{3+}	8.054	0.0369	0.0150	0.5	1.0
Er^{3+}	−5.206	0.0486	0.0136	−0.3	0.9
Yb^{3+}	168.858	0.1338–2.0102	0.0187	0.8–1.0	10.1–12.7
		A_4 (Ka_o^4)	A_6 (Ka_o^6)	b_4 (K)	b_6 (mK)
Dy^{3+}		−90.4	5.9	−0.626	−43.8
Er^{3+}		−92.3	4.9	−0.534	−29.4
Yb^{3+}		−89.5	0.2–3.5	−0.394	−0.938––14.1

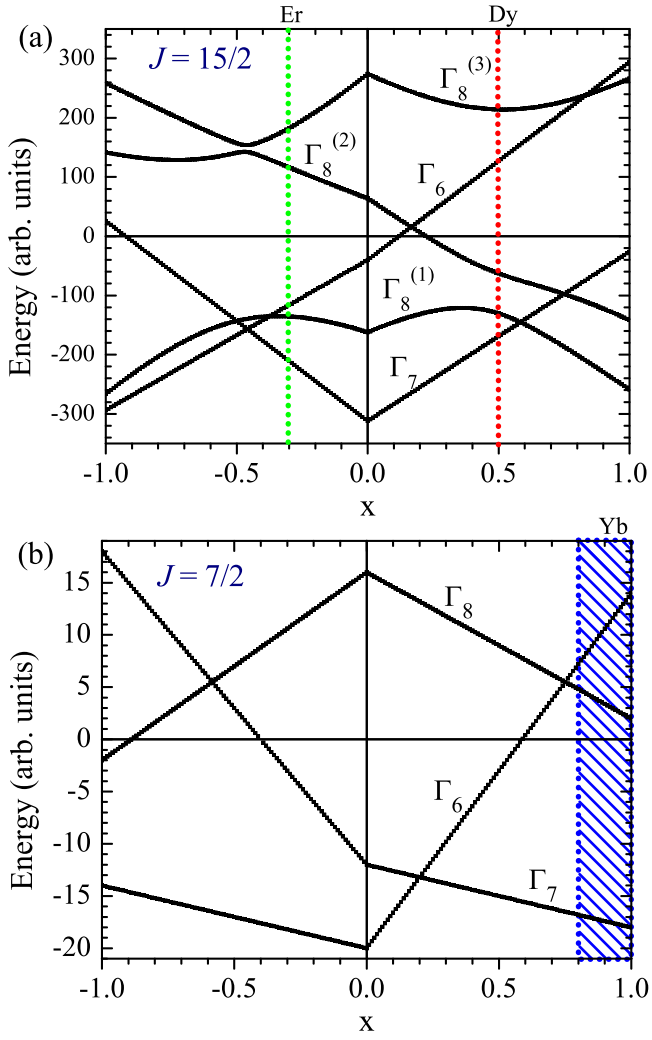

FIG. 8. Lea, Leask, and Wolf diagrams for (a) $J = 15/2$ and (b) $J = 7/2$. Green, red, and blue dotted lines indicate the energy level arrangement for the Er^{3+}, Dy^{3+}, and Yb^{3+} ions due to the CEF effect, respectively.

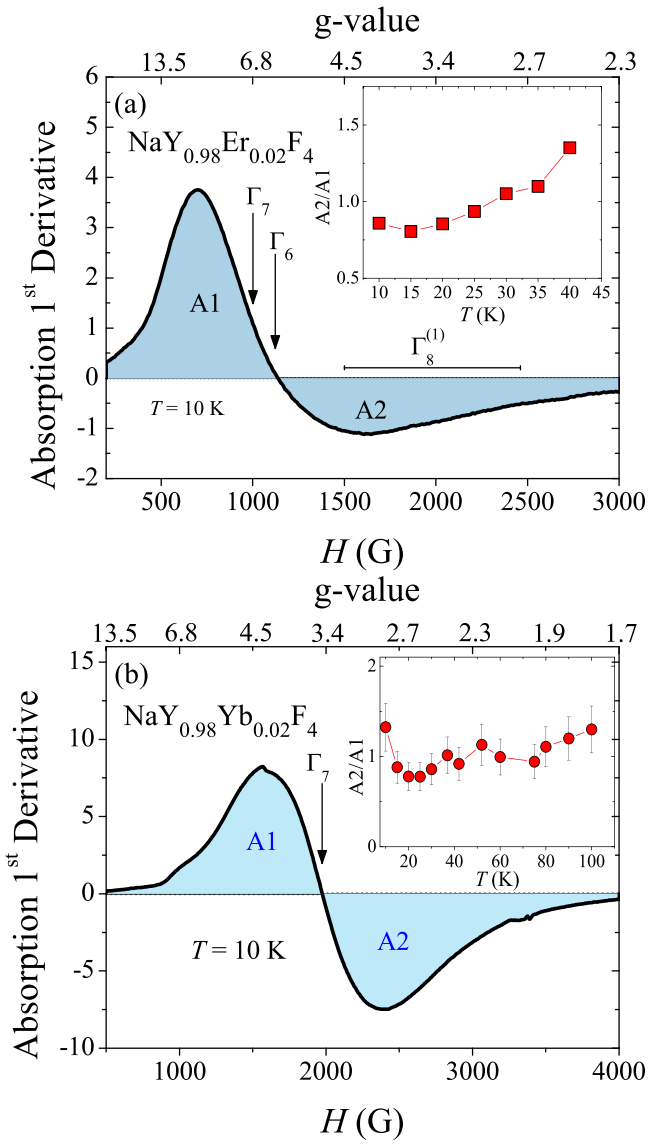

FIG. 9. (a) Deconvoluted ESR spectrum at 10 K of $NaY_{0.98}Er_{0.02}F_4$ and (b) $NaY_{0.98}Yb_{0.02}F_4$ NPs. A_1 and A_2 represent areas underneath the curve. Insets show the increase of the A_2/A_1 ratio with temperature for $T \geqslant 10$ K.

observed at low-T for the Er^{3+} and Dy^{3+} doped NPs [see Fig. 5(a) and 5(b)]. Thus, this asymmetry may come from transitions within the $\Gamma_8^{(1)}$ excited state of anisotropic g-values from ∼2 to ∼6 but with much lower intensities than the transitions within the Γ_7 ground state. However, for Yb^{3+} doped NPs the excited state Γ_8 is far from the Γ_7 ground state, leading to a near Lorentzian-like resonance at all temperatures [see Figs. 7 and 5(c)].

The conclusions obtained through the magnetization and susceptibility analysis are also supported by our ESR results. Figure 9(a) presents the ESR observed at 10 K for the Er^{3+} doped NPs as a function of the g-value (top scale) and the magnetic field (bottom scale). The main contribution to this spectrum comes from the g-value at ∼6.8 corresponding to the Γ_7 transition. The contributions from lower g-values (higher fields) are associated to the resonances within the anisotropic Γ_8 and isotropic Γ_6 excited states. Therefore, it is expected that for g-values between 2 and 6 there should be an almost continuum distribution of g-values due to the randomly dispersed NPs in toluene. Furthermore, the inset of Fig. 9(a) shows an increase of the relative ratio with temperature, A_2/A_1, between the areas underneath of the resonance above $T \geqslant 20$ K. This indicates that the increasing relative weight of the high field part of the ESR spectrum (lower g-values), may be attributed to the contribution of ESR resonances within the next anisotropic $\Gamma_8^{(1)}$ excited state. Notice that the upturn of A_2/A_1 is around 20 to 30 K (14-21 cm^{-1}) where the $\Gamma_8^{(1)}$ excited state starts to be thermally populated (see Fig. 7). In the case of Dy^{3+}, as Fig. 5(a) already shows, between 1.5 and 3 kG at low-T the presence of resonance lines that may be attributed to a nearby Γ_8 first excited state. The Yb^{3+} doped NPs, unlike those of Er^{3+} and Dy^{3+}, show a nearly symmetric Lorentzian-like ESR signal with a well-defined resonance g-value ∼3.4 [see Fig. 5(c) and Fig. 9(b)] compatible with an almost unaffected Γ_7 ground state.

TABLE III. Calculated and experimental linewidths of the UC light emission spectrum for Er^{3+}.

Transition	Calc (cm^{-1})	Exp (cm^{-1})
$^4F_{9/2} \rightarrow {}^4I_{15/2}$	390	507(28)
$^4S_{3/2} \rightarrow {}^4I_{15/2}$	309	452(28)
$^2H_{11/2} \rightarrow {}^4I_{15/2}$	423	417(28)

So far, only the analysis of the J-multiplet ground state, $^4I_{15/2}$ for Er^{3+} and Dy^{3+} and $^4F_{7/2}$ for the Yb^{3+} doped NPs, was considered. However, for the optical transitions, a detailed examination of the J-multiplet excited states is required. Figure 6 shows the room temperature UC light emission spectrum for the Er^{3+} and Yb^{3+} codoped cubic $NaYF_4$ NPs. Our spectrum is in agreement with that reported in the literature [22]. We also found that the UC light emission linewidth in the α-phase is broader than that for the β-phase NPs [13]. A fingerprint of the effect of the CEF on the emission spectra is seen on the $^4S_{3/2} \rightarrow {}^4I_{15/2}$ transition. The initial $^4S_{3/2}$ state has zero orbital angular moment and so it should show a small splitting under the influence of its neighborhood [23]. The width of this transition relates mostly to the ground-state splitting. The full width at half maximum for the $^4S_{3/2} \rightarrow {}^4I_{15/2}$ transition is around 452 cm^{-1} (Table III), close to the 263 cm^{-1} span by the ground-state multiplet (Table I). Therefore, we believe that the broadening and the multiple peaks present in the UC emission spectrum are, basically, due to crystal-field Stark splitting of each J-multiplet. The CEF breaks the degeneracy of these energy levels and then multiple transitions may occur that broaden the observed UC light emission.

To see the effect of the crystal field previously determined on the light emission we consider the full Hilbert space for the $4f^{11}$ electrons present on Er^{3+} [13]. The electron Hamiltonian includes now the free-ion (FI) and crystal field (CF) interaction

$$H = H_{\mathrm{FI}} + H_{\mathrm{CF}}. \tag{8}$$

Here, the single electron crystal field is given by

$$H_{\mathrm{CF}} = \sum_i b_4^0\left[O_4^0(i) + 5O_4^4(i)\right] + b_6^0\left[O_6^0(i) - 21O_6^4(i)\right], \tag{9}$$

where i varies over all electrons and the Stevens' operators are for the orbital magnetic momentum of single electrons. Similarly, the b_m^n parameters refer to single $l = 3, 4f$ electron CF parameters. These parameters are related to those obtained in a given J-multiplet by [16]

$$A_n^m = \frac{1}{\langle r^n\rangle\theta_{l,n}} b_n^m, \tag{10}$$

and are presented in Table II. The values of $\theta_{l,n}$ for $l = 2, 4, 6$ are given in Ref. [16] as α, β, and γ, respectively. The free-ion Hamiltonian is

$$H_{\mathrm{FI}} = \sum_{k=2,4,6} F^k f_k + \zeta_{4f} \sum_i \vec{l}_i \cdot \vec{\sigma}_i + \alpha L(L+1) + \beta G(R_2) + \gamma G(R_7). \tag{11}$$

TABLE IV. Free-ion parameters for Er^{3+} adapted from Ref. [28] (in K).

F^2	F^4	F^6	ζ_{4f}	α	β	γ
621.549	97.4042	10.7275	3493.81	26.5557	−879.29	1121.75

The electrostatic interaction is parameterized by F^2, F^4, and F^6 while ζ_{4f} accounts for the spin-orbit interaction [24–26]. We also included the configuration interaction terms proportional to α, β, and γ [27] (see Table IV). These parameters depend on the environment [28–30] and were adjusted to better fit the energy levels corresponding to the RE in this cubic compound.

TABLE V. Excited energy levels of Er^{3+} with CEF parameters obtained from best fits of low-T magnetization. Experimental values were estimated from UC light emission. All energies are in units of cm^{-1} and the zero energy was assigned to the ground state $^4I_{15/2}$.

Energy level	E (calc)		E (exp)
$^4I_{15/2}$	Doublet	0	0
	Quadruplet	56	
	Doublet	70	
	Quadruplet	260	
	Quadruplet	309	
$^4I_{13/2}$	Doublet	6727	
	Quadruplet	6730	
	Quadruplet	6847	
	Doublet	6852	
	Doublet	6855	
$^4I_{11/2}$	Quadruplet	10 448	
	Doublet	10 504	
	Quadruplet	10 505	
	Doublet	10 510	
$^4I_{9/2}$	Doublet	12 470	
	Quadruplet	12 614	
	Quadruplet	12 718	
$^4F_{9/2}$	Quadruplet	15 247	∼15 291
	Doublet	15 268	
	Quadruplet	15 328	
$^4S_{3/2}$	Quadruplet	18 409	∼18 071
$^2H\,{}^4G_{11/2}$	Quadruplet	19 303	∼19 461
	Doublet	19 310	
	Quadruplet	19 384	
	Doublet	19 418	
$^4F_{7/2}$	Doublet	20 317	
	Doublet	20 331	
	Quadruplet	20 398	
$^4F_{5/2}$	Doublet	22 003	
	Quadruplet	22 020	
$^4F_{3/2}$	Quadruplet	22 424	
$^2H\,{}^2G\,{}^4F_{9/2}$	Doublet	24 735	
	Quadruplet	24 849	
	Quadruplet	24 934	

The computed energy levels for Er^{3+} are shown in Table V up to the $^2H_{9/2}$ state. The observed radiative processes in the range of 500–700 nm (see Table III and Fig. 6) all involve the lowest-energy multiplet $^4I_{15/2}$. As shown previously, the CEF splits these ground multiplet states in a range of $\sim$263 cm^{-1}. So the emission widths should be at least $\sim$263 cm^{-1}, as is effectively seen (Table III). Notice that the full atomic Hamiltonian [Eq. (8)] gives a somewhat larger split for the ground-state multiplet of 309 cm^{-1} compared with that shown in Table I as a consequence of the interaction between the ground-state multiplet and the excited ones. The CEF also splits the excited states $^4F_{9/2}$, $^4S_{3/2}$, and $^2H_{11/2}$ resulting in a larger energy range for the light emission, in good agreement with the experimental observation.

At zero external magnetic field the whole linewidth is due to Stark and relaxation effects. The Stark splitting is found from the CEF fitting of the thermodynamic properties and varies between 306 cm^{-1} and 417 cm^{-1}, while the relaxation contribution is around or less than 139 cm^{-1}. The relaxation value is estimated from the difference between our computed linewidths and the experimentally observed value (Table III). The relaxation mechanism will be always present and probably temperature dependent. An external magnetic field or deformation can have a significant influence on the linewidths. The present model allows us to quantify the effect of an external magnetic field. We find that the linewidths increase as 9, 8, and 10 cm^{-1}/T for the transitions from $^4F_{9/2}$, $^4S_{3/2}$, and $^2H\,^4G_{11/2}$ to $^4I_{15/2}$, respectively.

VI. SUMMARY

Dy^{3+}, Er^{3+}, and Yb^{3+} doped α-phase $NaYF_4$ NPs of 8 nm mean size were successfully synthesized. The CEF analysis of the dc-magnetization data determined the CEF B_n^m parameters that allowed to evaluate the ground-state J-multiplet for each RE ion. These results were in good agreement with the results of ESR measurements, where a Kramers' doublet Γ_7 was found as the ground state in the NPs doped with Dy^{3+}, Er^{3+}, and Yb^{3+} ions. The UC light emission spectrum for Er-doped $NaYF_4$ was calculated using the same CEF B_n^m parameters obtained from the magnetization analysis. The linewidths computed for the Er ion diluted in the cubic host lattice is in very good agreement with the experimental UC light emission results.

In summary, we showed that it was possible to obtain the internal structure of high-energy multiplets of Er and Yb doped α-$NaYF_4$ NPs by means of dc-magnetization, optical, and microwave quantum mechanic spectroscopic techniques involving the Stark and Zeeman effects.

ACKNOWLEDGMENTS

This work was supported and performed under the auspices of the Brazilian agencies CAPES, CNPq, and FAPESP through Grants No. 2017/10581-1, No. 2018/21025-5, and No. 2015/23882-4. A.F.G.-F. is the beneficiary of a FAPESP fellowship Grant No. 2019/09673-4. R.R.U. also acknowledges the National Council for Scientific and Technological Development (CNPq) Grants No. 309483/2018-2 and No. 314587/2021-7. F.F. is the beneficiary of a postdoctoral FAPESP fellowship Grant No. 2019/13678-1. D.J.G. acknowledges support from PICT 2019-02396 of the ANPCyT and PIP 11220200101796CO of CONICET. P.S.C. acknowledges support from Grants No. PICT 2018-01546 and No. PICT 2019-00371 of the ANPCyT. Research supported by LNNano–Brazilian Nanotechnology National Laboratory (CNPEM/MCTI) during the use of the electron microscopy open access facility. The authors acknowledge the support of the multiuser experiment center at UFABC, especially on the magnetization measurements.

[1] C. G. Granqvist, R. A. Buhrman, J. Wyns, and A. J. Sievers, Phys. Rev. Lett. **37**, 625 (1976).
[2] E. D. Martínez, C. D. S. Brites, L. D. Carlos, A. F. García-Flores, R. R. Urbano, and C. Rettori, Adv. Funct. Mater. **29**, 1807758 (2019).
[3] E. D. Martínez, A. F. García-Flores, A. N. Carneiro Neto, C. D. S. Brites, L. D. Carlos, R. R. Urbano, and C. Rettori, Nanoscale **13**, 16267 (2021).
[4] B. Dong, S. Xu, J. Sun, S. Bi, D. Li, X. Bai, Y. Wang, L. Wang, and H. Song, J. Mater. Chem. **21**, 6193 (2011).
[5] H. X. Mai, Y. W. Zhang, L. D. Sun, and C. H. Yan, J. Phys. Chem. C **111**, 13721 (2007).
[6] Y. Zhao and S. Fleming, Electron. Lett. **32**, 1199 (1996).
[7] E. D. Martínez, R. R. Urbano, and C. Rettori, Nanoscale **10**, 14687 (2018).
[8] G. Dumlupinar, Crystal structure and luminescence studies of upconverting nanoparticles, MA thesis, Lund Univeristy, 2015.
[9] F. Frenzel, C. Würth, O. Dukhno, F. Przybilla, L. M. Wiesholler, V. Muhr, T. Hirsch, Y. Mély, and U. Resch-Genger, Nano Res. **14**, 4107 (2021).
[10] M. D. Wisser, ACS Photonics **3**, 1523 (2016).
[11] L. Yao, Y. Li, D. Xu, H. Lin, Y. Peng, S. Yang, and Y. Zhang, J. Lumin. **211**, 144 (2019).
[12] H. A. Bethe, Ann. Phys. Lpz. **3**, 133 (1929).
[13] A. F. García-Flores, J. S. Matias, D. J. Garcia, E. D. Martínez, P. S. Cornaglia, G. G. Lesseux, R. A. Ribeiro, R. R. Urbano, and C. Rettori, Phys. Rev. B **96**, 165430 (2017).
[14] K. R. Lea, M. J. M. Leask, and W. P. Wolf, J. Phys. Chem. Solids **23**, 1381 (1962).
[15] M. T. Hutchings, Solid State Phys. **16**, 227 (1964).
[16] K. W. H. Stevens, Proc. Phys. Soc. A **65**, 209 (1952).
[17] D. Tu, Y. Liu, H. Zhu, R. Li, L. Liu, and X. Chen, Angew. Chem. **125**, 1166 (2013).
[18] H. X. Mai, Y. W. Zhang, L. D. Sun, and C. H. Yan, J. Am. Chem. Soc. **128**, 6426 (2006).
[19] P. Scherrer, Mathematisch-Physikalische Klasse **2**, 98 (1918).
[20] R. J. Elliott and K. W. H. Stevens, Proc. R. Soc. London A **219**, 387 (1953).
[21] A. Freeman and R. Watson, Phys. Rev. **127**, 2058 (1962).
[22] S.-N. Shan, X.-Y. Wang, and N.-Q. Jia, Nanoscale Res. Lett. **6**, 539 (2011).

[23] D. Betancourth, V. F. Correa, J. I. Facio, J. Fernández, V. Vildosola, R. Lora-Serrano, J. M. Cadogan, A. A. Aligia, P. S. Cornaglia, and D. J. García, Phys. Rev. B **99**, 134406 (2019).
[24] J. C. Eisenstein, J. Chem. Phys. **39**, 2134 (1963).
[25] G. H. Dieke and H. M. Crosswhite, Appl. Opt. **2**, 675 (1963).
[26] E. U. Condon and G. H. Shortley, *The Theory of Atomic Spectra* (Cambridge University Press, Cambridge, England, 1951).
[27] K. Rajnak and B. G. Wybourne, Phys. Rev. **132**, 280 (1963).
[28] W. T. Carnall, P. R. Fields, and K. Rajnak, J. Chem. Phys. **49**, 4424 (1968).
[29] W. T. Carnall, G. L. Goodman, K. Rajnak, and R. S. Rana, J. Chem. Phys. **90**, 3443 (1989).
[30] G. H. Dieke, H. M. Crosswhite, H. Crosswhite, *Spectra and Energy Levels of Rare Earth Ions in Crystals* (Interscience, New York, 1968).